Composites Part B 248 (2023) 110381

Contents lists available at ScienceDirect

Composites Part B

journal homepage: www.elsevier.com/locate/compositesb

Delamination measurement in glass fibre reinforced polymer (GFRP) composite based on image differencing☆

Tamás Lukács, Csongor Pereszlai, Norbert Geier *

Budapest University of Technology and Economics, Faculty of Mechanical Engineering, Department of Manufacturing Science and Engineering, Müegyetem rkp. 3., Budapest, 1111, Hungary

ARTICLE INFO

Keywords:
Polymer-matrix composites
Delamination
Optical microscopy
Machining

ABSTRACT

Drilling-induced delamination is the most severe material defect in fibrous polymeric composites. Although many delamination measurement methods are available, the outputs of recent digital image processing (DIP) based delamination measurement methods are significantly affected by the non-drilling induced material defects and anomalies like cavities or dirty textured surfaces. Therefore, the main aim of the present research was to develop a method capable of drilling-induced delamination measurement in fibrous polymeric composites based on the image differentiation principle. In an attempt to implement this principle, images of the undrilled composites were referenced/compared with the images of the drilled composites. The proposed delamination measurement method is tested through mechanical drilling experiments in glass fibre reinforced polymer (GFRP) composites and compared with conventional DIP-supported manual measurements. The experimental results show a good agreement between the delamination detected by the naked eye, the conventional and the proposed method. Although the proposed method slightly increases the drilling operation time, the comparative differentiating makes it a good solution to detect drilling-induced material deformations in textured and semi-specular surfaces. The proposed method can separate drilling-induced delamination from other non-drilling-induced material discontinuities or anomalies. Considering the automated, reproducible and complex nature of the novel method, it may replace current qualification operations in high-end industries.

1. Introduction

Fibre reinforced polymer (FRP) composites are widely used structural materials in high-end industries, mainly due to their superior specific mechanical properties [1–3]. Although these fibrous composites are often manufactured ready-to-shape by the industries, their post-machining is often necessary to meet dimensional requirements [4–9]. Glass fibre reinforced polymer (GFRP) composites are difficult-to-cut materials because of their inhomogeneous and anisotropic nature [10]. Inappropriate GFRP machining processes often result in fibrous composite-specific damages like delamination, burrs, fibre pull-outs, matrix smearing and tearing [11–13]. The delamination is one of the most serious damages in composites, as it reduces the resultant strength of the composite part directly [14,15]. Therefore, the present study focuses on measuring and quantifying drilling-induced delamination in GFRP composites.

Delamination forms if the loads on the composite plies exceed the interlaminar fracture toughness of the composite, resulting in layer separation, interlaminar cracks and material discontinuities [16]. Drilling-induced delamination in GFRPs may be observable at the entry and exit sides of the hole, called peel-up and push-out delamination, respectively [17]. The peel-up delamination results from the upward force component of the rake face of the drilling tool, while the push-out delamination is caused primarily by the pushing effect of the centre of the drilling tool. Consequently, the push-out delamination is often larger than the peel-up, as shown by Sorrentino et al. [18] and Lissek et al. [19]. According to Hocheng and Tsao [20], the larger the feed, the larger the thrust force; thus, the larger the push-out delamination in fibrous composites is. The cutting edge radius significantly affects the cutting force and chip removal mechanisms [21]; and the probability of delamination formation. The larger the cutting edge radius, the larger the ploughing effect is; thus, the cutting force is also larger in this case [22–24]. Therefore, the delaminated area is often larger at a larger

☆ 2212-8271 © 2020 The Authors. Published by Elsevier B.V. Peer-review under responsibility of the scientific committee of the 14th CIRP Conference on Intelligent Computation in Manufacturing Engineering.

* Corresponding author.
E-mail address: geier.norbert@gpk.bme.hu (N. Geier).

https://doi.org/10.1016/j.compositesb.2022.110381
Received 21 August 2022; Received in revised form 18 October 2022; Accepted 25 October 2022
Available online 28 October 2022

Nomenclature

A_{del}	Area of delamination (mm^2)
A_{max}	Area belonging to the maximum diameter of the delamination zone (D_{max}) (mm^2)
A_{nom}	The nominal area of the hole (mm^2)
DF	Two-dimensional delamination factor (%)
D_{max}	The maximum diameter of the delamination zone (mm)
D_{min}	The diameter of the circle around the delaminated zone (mm)
D_{nom}	The nominal diameter of the hole (mm)
f	Feed rate (mm/rev)
F'_d	Corrected delamination factor (%)
F_d	Conventional delamination factor (1)
$F_{d,inv}$	Inverse delamination factor (1)
F_{da}	Adjusted delamination factor (1)
F_{dmin}	Minimum delamination factor (1)
F_{ed}	Equivalent delamination factor (1)
R_d	Delamination size (1)
R_{max}	The maximum radius of the delamination zone (mm)
R_{nom}	The nominal radius of the hole (mm)
v_c	Cutting speed (m/min)
ξ	Threshold value for filtering (pixel)
CFRP	Carbon fibre reinforced polymer
CHT	Circular Hough transform
DIP	Digital image processing
DP	Delamination parameter
FRP	Fibre reinforced polymer
GFRP	Glass fibre reinforced polymer
MPD	Mean percentage difference (%)
SEC	Smallest enclosing circle
SSD	Sum of squared differences

cutting edge radius, which may be caused by inappropriate tool geometry or accelerated tool wear [25,26]. The improper mechanical supporting properties of the laminates also increase the probability of delamination formation; thus, the researchers recommend the application of a back-up support plate [27–29]. Despite the influences of the (i) process parameters, (ii) tool geometry, (iii) material properties and (iv) mechanical supporting properties on the delamination formation mechanisms are extensively investigated, the delamination suppression and prediction are still a challenging task in the industry and academia [14,30].

Drilling-induced delamination can be characterised by several simple and complex factors, as shown in Fig. 1 and summarised in Table 1. The conventional delamination factor (F_d) is the most widely used quality indicator, as it is easy to calculate and implement [31]. Although the conventional delamination factor is often useable, more complex measures were proposed by the researchers to provide information not only on the relative size of the delaminated area but also on the shape [19,32]. Determination of each parameter listed in Table 1 requires two-dimensional geometrical information on the damaged feature properties at the entry and exit sides of the holes. This information is often collected by manual measurements [33–40] or digital image processing (DIP) of images taken by an optical microscope [16,18,32,41] and C-scan [42–45].

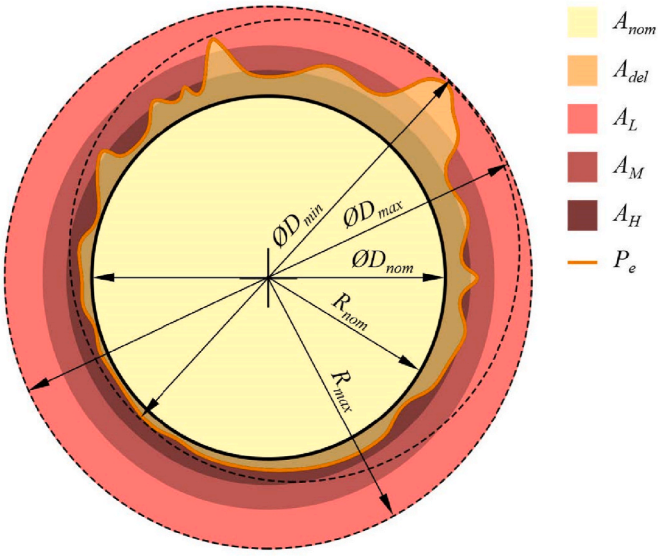

Fig. 1. Schematic diagram for the interpretation of main geometrical features related to delamination metrics [46].

Table 1
List of parameters characterising machining-induced delamination in fibrous polymer composites.

Name	Dimension	Equation	Reference
Conventional delamination factor	1	$F_d = \frac{D_{max}}{D_{nom}}$	Chen [47]
Corrected delamination factor	%	$F'_d = \frac{(D_{max} - D_{nom})}{D_{nom}} \cdot 100$	Gaugel et al. [16]
Inverse delamination factor	1	$F_{d,inv} = \frac{D_{nom}}{D_{max}}$	Khanna et al. [48]
Minimum delamination factor	1	$F_{dmin} = \frac{D_{min}}{D_{nom}}$	Da Silva [49]
Two-dimensional delamination factor	%	$DF = \left(\frac{A_{del}}{A_{nom}}\right)\%$	Faraz et al. [50]
Adjusted delamination factor	1	$F_{da} = F_d + \frac{A_{del}}{(A_{max} - A_{nom})} \cdot (F_d^2 - F_d)$	Davim et al. [32]
Equivalent delamination factor	1	$F_{ed} = \frac{\sqrt{\frac{4 \cdot (A_{del} + A_{nom})}{\pi}}}{D_{nom}}$	Tsao et al. [51]
Delamination size	1	$R_d = R_{max} - R_{nom}$	Khashaba [52]

Most published digital image processing algorithms are based on contrast and edge detection of optically captured images on the delaminated area. Davim et al. [32] developed a DIP method to measure and qualify visibly drilling-induced delamination in multidirectional carbon fibre reinforced polymer (CFRP) composites. They processed the images in Image J software by properly setting a series of parameters like brightness intensity, noise reduction, image enhancement, and edge detection. Sorrentino et al. [18] successfully adapted the DIP method of Davim et al. and concluded that the detected delamination correlates well to the visibly damaged area around the drilled holes in CFRPs. Gaugel et al. [16] drilled holes in CFRPs and examined their quality by the DIP of microscopic images. They used different illumination concepts and a pixel segmentation process using the Zeiss AxioVision software. For the delamination parameter calculations, they had to manually draw an ellipse to the edge of the drilled hole. They concluded that their novel DIP algorithm is suitable for quantifying the borehole quality considering the damaged area and shape. Considering that digital processing of images of fibrous materials is challenging mainly due to the textured and semi-specular surfaces (as illustrated in Fig. 2), Maghami et al. [53] developed a novel method to inspect drilling-induced damages using multi-light imaging and deep learning methods. They captured images at different lightning directions, then fused them to increase the contrast between the damages and the

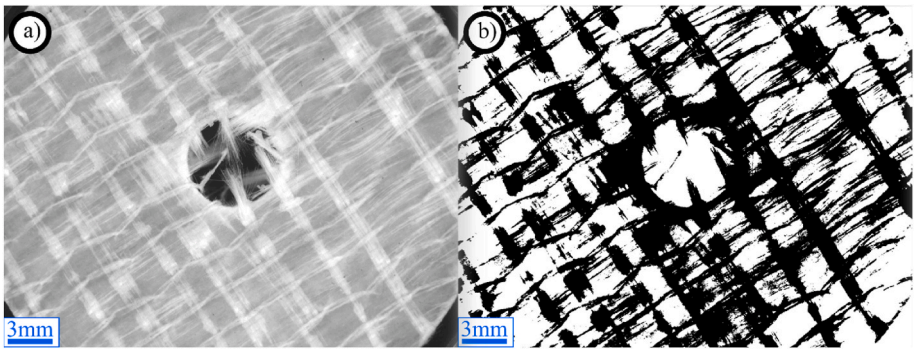

Fig. 2. Textured and semi-specular surfaces of GFRP composites make the digital image processing challenging: (a) original image on GFRP, (b) segmented image that is highly noise-loaded.

background. By this novel solution, they could develop a fully-automatised hybrid DIP and machine learning process that is able to measure and quantify damages in CFRPs.

Although the published drilling-induced delamination measurement DIP algorithms being useable, these are difficult to reproduce because the developed algorithms are not presented fully and need considerable manual input. These challenges make these methods difficult to implement and automatise. Therefore, the main aim of the present study is to develop a novel method to measure drilling-induced delamination in GFRP composites based on the different light reflection properties of the composite before and after the drilling, using the image differencing principle. The novel algorithm is presented in **Section 2**. The applicability of the method was tested through drilling experiments, as presented in **Section 3**. Finally, the results are presented and discussed in **Section 4**.

2. Description of the proposed delamination measurement method

The drilling-induced delaminated areas in the GFRP composite appear to whiten, which is explained by the change in the refractive index of the material. This phenomenon allows us to measure the magnitude of delamination through digital image processing. However, measuring delamination is challenging with conventional image processing methods because the light reflection of the reinforcing fibres – that densely cross the workpiece – is difficult to distinguish from the delaminated areas, as explained in the introduction (Fig. 2). Therefore, a novel approach is developed in this study to detect and measure drilling-induced delaminated area more accurately, simpler, and faster. This new method is based on the principle of image differencing [54]. To implement this principle, images of the undrilled composites were referenced/compared with those of the drilled composites. Images are taken of the workpiece both before (Fig. 3a) and after drilling (Fig. 3b) so that changes caused by drilling can be detected by comparing the images.

The main steps of the proposed drilling-induced delamination measurement method are illustrated in Fig. 4 and Fig. 5, and detailed as follows:

(i) Capture high-resolution grayscale images of the workpiece before and after drilling using a digital microscope. The conditions for capturing must be the same for both images. The pixels of the image taken before drilling are collected in the matrix $\boldsymbol{B}_{ij}$, and the pixels taken after drilling are collected in the matrix $\boldsymbol{A}_{ij}$, where i denotes the rows and j denotes the columns of the pixels. The matrices are formulated as expressed by **Eq. (1)** and **Eq. (2)**. This step is illustrated in Fig. 5a and b.

$$\boldsymbol{B}_{ij} = \begin{pmatrix} b_{11} & \cdots & b_{1m} \\ \vdots & \ddots & \vdots \\ b_{n1} & \cdots & b_{nm} \end{pmatrix}; b_{ij} \in (0, 1 \ldots 255) \tag{1}$$

$$\boldsymbol{A}_{ij} = \begin{pmatrix} a_{11} & \cdots & a_{1m} \\ \vdots & \ddots & \vdots \\ a_{n1} & \cdots & a_{nm} \end{pmatrix}; a_{ij} \in (0, 1 \ldots 255) \tag{2}$$

(ii) Align the images using intensity-based image registration. The first step of this method is to take the two images and overlap them as

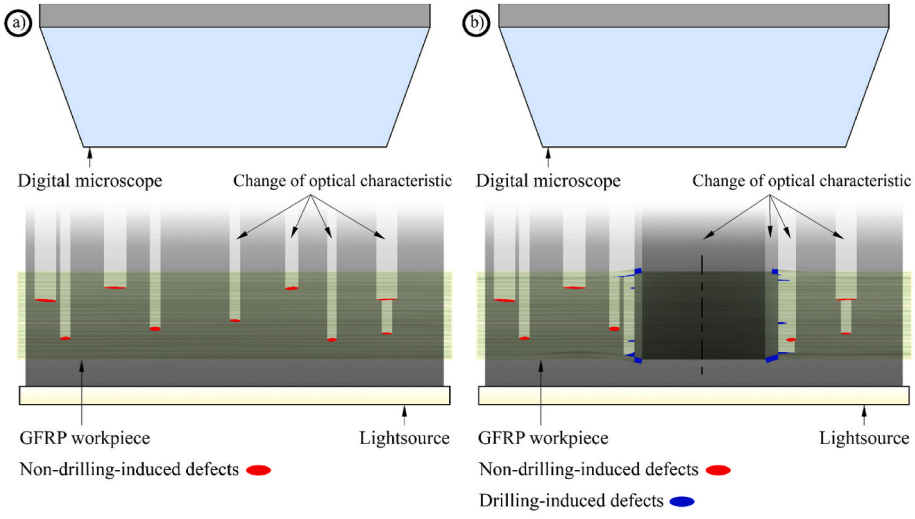

Fig. 3. Glass fibre reinforced polymer (GFRP) composite (a) before and (b) after mechanical drilling operation provides enough information to differentiate whether a material defect is induced by the drilling operation.

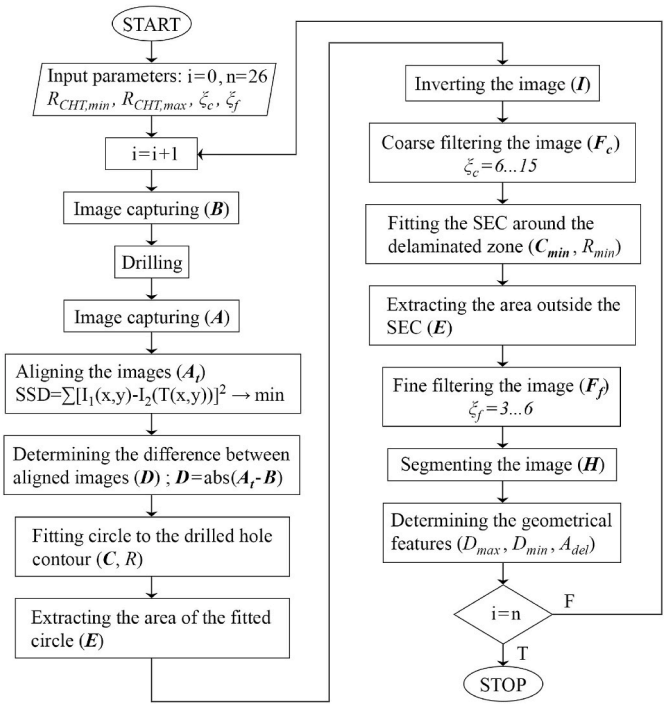

Fig. 4. Flowchart of the proposed drilling-induced delamination detection method in GFRPs.

they are. Then, we have to compute some similarity between them based on the intensity map of the images. To define this similarity, calculate the sum of squared differences (SSD) for the overlapped pixels as expressed by Eq. (3). The goal is to minimise the value of this similarity metric. Perform geometrical transformations on the image captured after drilling ($\boldsymbol{A}_{ij}$) until the global minimum of this metric is found, which means that the images are aligned optimally. These geometrical transformations can be translations, rotations and scaling (if necessary). The pixels of the optimally transformed (aligned) image are collected in the matrix $\boldsymbol{A}_{Tij}$, expressed by Eq. (4). This step is illustrated in Fig. 5c.

$$SSD = \sum_{i=1}^{n}\sum_{j=1}^{m}\left[b_{ij} - a_{ij}\right]^2 \rightarrow min \tag{3}$$

$$\boldsymbol{A}_{Tij} = \begin{pmatrix} a_{T11} & \cdots & a_{T1m} \\ \vdots & \ddots & \vdots \\ a_{Tn1} & \cdots & a_{Tnm} \end{pmatrix}; a_{Tij} \in (0, 1\ldots255) \tag{4}$$

(iii) Determine the difference between aligned ($\boldsymbol{A}_{Tij}$) and reference image ($\boldsymbol{B}_{ij}$). Since images are interpreted as matrices – where each matrix element contains the grayscale value (between 0 and 255) of a given pixel – the difference between the images can be defined as the subtraction of matrices. In order to avoid any element with a negative grayscale value, take the absolute value of the subtraction. The pixels of the difference image are collected in matrix $\boldsymbol{D}_{ij}$, expressed by Eq. (5) and Eq. (6). This step is illustrated in Fig. 5d.

$$\boldsymbol{D}_{ij} = abs\left(\boldsymbol{A}_{Tij} - \boldsymbol{B}_{ij}\right) \tag{5}$$

$$\boldsymbol{D}_{ij} = \begin{pmatrix} d_{11} & \cdots & d_{1m} \\ \vdots & \ddots & \vdots \\ d_{n1} & \cdots & d_{nm} \end{pmatrix}; d_{ij} \in (0, 1\ldots255) \tag{6}$$

(iv) Fit a circle to the drilled hole contour. Estimate the radius of the circle to be detected by manual measurement, then find the circle with an uncertainty of 2% relative to this estimated radius value using a circular Hough transform (CHT) [55]. With this step, the centre $\boldsymbol{C}_{ij}$ and the radius R of the fitted circle are obtained, expressed by Eq. (7), where c_{11} and c_{12} denote the coordinates of the fitted circle in the difference image ($\boldsymbol{D}_{ij}$). This step is illustrated in Fig. 5e.

$$\boldsymbol{C}_{ij} = (c_{11}, c_{12}) \tag{7}$$

(v) Extract the area of the fitted circle from the image. If the distance between a pixel in the difference image ($\boldsymbol{D}_{ij}$) and the centre of the fitted circle $\boldsymbol{C}_{ij}$ is smaller than the radius R, it becomes black; otherwise, it remains the same. The pixels of the image from which the area of the fitted circle is extracted are collected in matrix $\boldsymbol{E}_{ij}$, expressed by Eq. (8) and Eq. (9), where i denotes the rows and j denotes the columns of the pixels, and n denotes the number of rows and m denotes the number of columns. This step is illustrated in Fig. 5f.

$$e_{ij} = \begin{cases} 0, \sqrt{(i-c_{11})^2 + (j-c_{12})^2} < R \\ d_{ij}, \sqrt{(i-c_{11})^2 + (j-c_{12})^2} \geq R \end{cases}; i = 1, \ldots, n\ ;\ j = 1, \ldots, m \tag{8}$$

$$\boldsymbol{E}_{ij} = \begin{pmatrix} e_{11} & \cdots & e_{1m} \\ \vdots & \ddots & \vdots \\ e_{n1} & \cdots & e_{nm} \end{pmatrix}; e_{ij} \in (0, 1\ldots255) \tag{9}$$

(vi) Invert the image. Create a matrix with the same size as the matrix

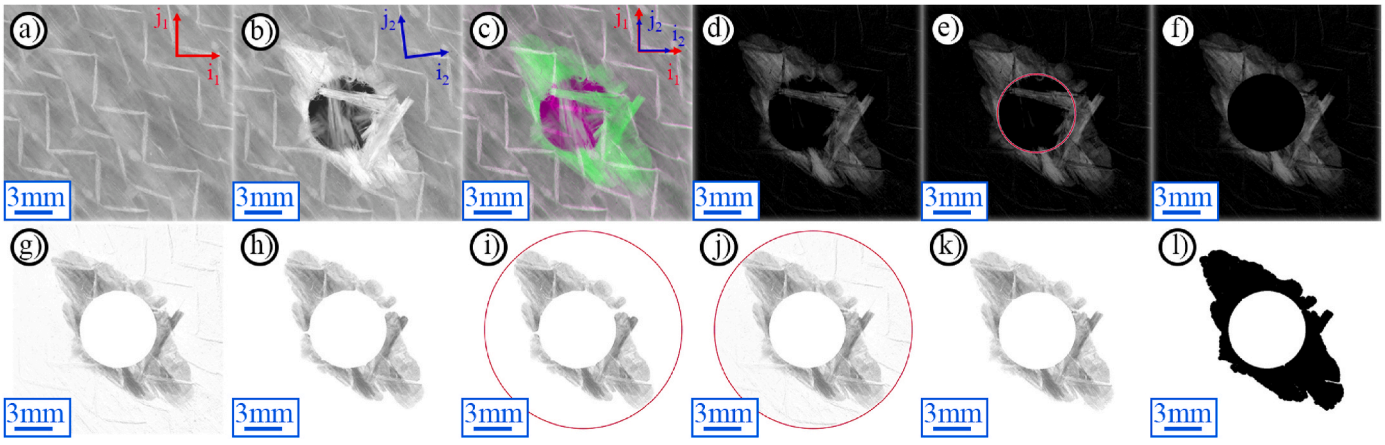

Fig. 5. (a) Image capturing before drilling, (b) Image capturing after drilling, (c) Aligning pre- and post-drill images, (d) Determining the difference between the aligned images, (e) Fitting circle to the drilled hole contour, (f) Extracting points enclosed by the fitted circle, (g) Inverting the image, (h) Filtering the image (coarse), (i) Determining the SEC of the delamination zone, (j) Extracting points outside the SEC from the inverted image, (k) Filtering the image (fine), (l) Segmenting the image.

$\boldsymbol{E_{ij}}$, but all elements are equal to 255. Then subtract the matrix $\boldsymbol{E_{ij}}$ from this matrix. The pixels of the inverted image are collected in matrix $\boldsymbol{I_{ij}}$, expressed by Eq. (10). This step is justified for practical reasons. This step is illustrated in Fig. 5g.

$$\boldsymbol{I}_{ij} = \begin{pmatrix} 255 - e_{11} & \cdots & 255 - e_{1m} \\ \vdots & \ddots & \vdots \\ 255 - e_{n1} & \cdots & 255 - e_{nm} \end{pmatrix} = \begin{pmatrix} i_{11} & \cdots & i_{1m} \\ \vdots & \ddots & \vdots \\ i_{n1} & \cdots & i_{nm} \end{pmatrix}; i_{ij} \in (0, 1 \ldots 255) \tag{10}$$

(vii) Filter the inverted image ($\boldsymbol{I_{ij}}$) based on the size of the contiguous areas using a high-pass filter. Choose a threshold of $\xi_c = 6 \ldots 15$ that just eliminates any noise outside the delaminated area. As a result, the delaminated area also becomes thinner, which is unfavourable. Three additional steps (viii, ix and x) are introduced to reduce this side effect. The pixels of the – coarse – filtered image are collected in matrix $\boldsymbol{F_{Cij}}$, expressed by Eq. (11). This step is illustrated in Fig. 5h.

$$\boldsymbol{F}_{Cij} = \begin{pmatrix} f_{C11} & \cdots & f_{C1m} \\ \vdots & \ddots & \vdots \\ f_{Cn1} & \cdots & f_{Cnm} \end{pmatrix}; f_{Cij} \in (0, 1 \ldots 255) \tag{11}$$

(viii) Fit the smallest enclosing circle (SEC) around the delaminated zone in the filtered image ($\boldsymbol{F_{Cij}}$). In order to find the SEC, all possible locations of the centre of the circle must be examined. For each pixel, determine the distance between that pixel and the non-white pixel farthest from it, and collect these values in the matrix $\boldsymbol{X_{ij}}$, expressed by Eq. (12) and Eq. (13). The value of the smallest element of the matrix $\boldsymbol{X_{ij}}$ is equal to the radius $\boldsymbol{R_{min}}$ of the SEC, and the centre $\boldsymbol{C_{min}}$ of the SEC is obtained by the coordinates of this matrix element, expressed by Eq. (14) and Eq. (15). This step is illustrated in Fig. 5i.

$$x_{ij} = \max_{f_{Cpq}<255} \left(\sqrt{(p-i)^2 + (q-j)^2} \right);\ i = 1, \ldots, n; j = 1, \ldots, m \tag{12}$$

$$\boldsymbol{X}_{ij} = \begin{pmatrix} x_{11} & \cdots & x_{1m} \\ \vdots & \ddots & \vdots \\ x_{n1} & \cdots & x_{nm} \end{pmatrix}; x_{ij} \in \mathbb{R}^+;\ i = 1, \ldots, n; j = 1, \ldots, m \tag{13}$$

$$R_{min} = \min_{\substack{i \in \{1,\ldots,n\} \\ j \in \{1,\ldots,m\}}} \left(x_{ij} \right) \tag{14}$$

$$\boldsymbol{C_{min}} = \left(c_{min,11}\ , c_{min,12} \right) \tag{15}$$

(ix) Extract the area outside the smallest enclosing circle from the inverted image ($\boldsymbol{I}$). If the distance between a pixel in the inverted image ($\boldsymbol{I_{ij}}$) and the centre $\boldsymbol{C_{min}}$ of the SEC is greater than the radius R_{min}, it becomes white; otherwise, it remains the same. The pixels of the image from which the area outside the circle is extracted are collected in the matrix $\boldsymbol{G_{ij}}$, expressed by Eq. (16) and Eq. (17), where i denotes the rows and j denotes the columns of the pixels, and n denotes the number of rows and m denotes the number of columns. This step is illustrated in Fig. 5j.

$$g_{ij} = \begin{cases} 255, \sqrt{\left(i - c_{min,11}\right)^2 + \left(j - c_{min,12}\right)^2} > R_{min} \\ i_{ij}, \sqrt{\left(i - c_{min,11}\right)^2 + \left(j - c_{min,12}\right)^2} \le R_{min} \end{cases}; i = 1, \ldots, n;\ j = 1, \ldots, m \tag{16}$$

$$\boldsymbol{G}_{ij} = \begin{pmatrix} g_{11} & \cdots & g_{1m} \\ \vdots & \ddots & \vdots \\ g_{n1} & \cdots & g_{nm} \end{pmatrix}; g_{ij} \in (0, 1 \ldots 255) \tag{17}$$

(x) Repeat step (vii) using a smaller threshold ($\xi_f = 3 \ldots 6$) if it results in a more detailed image without noise appearing outside the delaminated area. The pixels of the – fine – filtered image are collected in matrix $\boldsymbol{F_{fij}}$, expressed by Eq. (18). This step is illustrated in Fig. 5k.

$$\boldsymbol{F}_{f_{ij}} = \begin{pmatrix} f_{f_{11}} & \cdots & f_{f_{1m}} \\ \vdots & \ddots & \vdots \\ f_{f_{n1}} & \cdots & f_{f_{nm}} \end{pmatrix}; f_{f_{ij}} \in (0, 1 \ldots 255) \tag{18}$$

(xi) Segment (*i.e.* binarise) the image for better visualisation. If the grayscale value of a pixel in the fine filtered image ($\boldsymbol{F_{fij}}$) is smaller than 255, it becomes black; otherwise, it remains the same (white). The pixels of the segmented image are collected in the matrix $\boldsymbol{H_{ij}}$, expressed by Eq. (19) and Eq. (20). This step is illustrated in Fig. 5l.

$$h_{ij} = \begin{cases} 0, f_{f_{ij}} > 255 \\ f_{f_{ij}}, f_{f_{ij}} = 255 \end{cases}; i = 1, \ldots, n;\ j = 1, \ldots, m \tag{19}$$

$$\boldsymbol{H}_{ij} = \begin{pmatrix} h_{11} & \cdots & h_{1m} \\ \vdots & \ddots & \vdots \\ h_{n1} & \cdots & h_{nm} \end{pmatrix}; h_{ij} \in (0, 1 \ldots 255) \tag{20}$$

(xii) Determine the geometrical features required to calculate delamination factors. Depending on the given method, these geometrical features can be radii, diameters, areas, and perimeters. The radius and diameter values are obtained by fitting the given circles using the least-squares method. The size of the delaminated area can be calculated by counting the black pixels belonging to the affected zone.

3. Experimental setup

In this study, eight-layer unidirectional glass fibre reinforced polymer (UD-GFRP) composite specimens were used which were made by vacuum bag moulding and then cut to size by water jet. The composites were constructed of NOVIA unidirectional glass fabric (surface mass of 440 g/m^2) embedded in an epoxy matrix (mixture of IPOX ER1010 resin and IPOX MH3124 hardener in the ratio of 100:35, respectively). The laminated specimens were cured for one day at room temperature, then post-cured for t = 4 h in an oven at T = 60 °C. The thickness of the specimens was manufactured to $h = 3.5$ mm and their outer diameter to $D_o = Ø34$ mm.

The drilling operations were performed on a VHTC-130 linear five-axis micromachining centre. The resulting chips were removed from the cutting zone using a NILFISK GB733 industrial vacuum cleaner. Two different tools were used for drilling: a Ø6 FRAISA 20360302 uncoated carbide drill (T1) and a Ø6 TIVOLY 82329710600 uncoated single flute carbide end mill (T2), illustrated in Fig. 6b and c, respectively. The composite specimens were fixed with a special fixture that provided symmetrical protection against buckling to minimise delamination and burr formation.

The experimental design was compiled using the central composite face-centred (CCF) experimental design method. Drilling experiments were performed at multiple feeds and cutting speeds and no coolant was used. Experimental factors and their levels were determined according

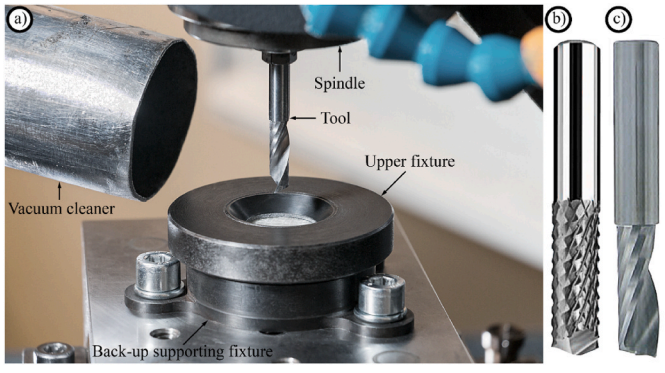

Fig. 6. Experimental setup: (a) drilling environment (b) uncoated carbide drill (c) uncoated single flute carbide end mill.

to the central composite design and based on other research works [27].

In order to ensure that the environmental effects do not systematically affect the experimental results, the order of the experiments was randomised. The factors and their levels can be seen in Table 2, and the randomised experimental design table is shown later in the appendices (Table A1 and Table A2).

Images of the specimens were captured by a telecentric Mitutoyo QI-A505 digital microscope (Fig. 7) before and after drilling. The microscope was used in dome lighting mode at 76% of its maximum illuminating power. Images were taken at 5× nominal magnification and 1280 x 960 pixels resolution. The microscopic images were evaluated in a Matlab environment using the image processing algorithm presented in **Section 2**.

4. Results and validation

In order to test the applicability of our proposed algorithm, mechanical drilling experiments were carried out in GFRP composite. A total number of 26 holes with a diameter of 6 mm were drilled by varied feed rates, cutting speeds and tools. Digital images were taken of both the entrance and exit sides of the holes both before and after the drilling operations. The digital images were evaluated by the proposed method (**Section 2**) and were compared by manual measurements. The manual measurements are based on only the images taken after the drilling operations and are supported by manual image manipulating tools, such as the threshold of segmentation and filtering. Although the manual delamination measurements are challenging to reproduce and automatise, their resulting delamination parameters are very close to the expected values, as the geometric feature detection based on the human naked eye is extremely precise and flexible [31,56]. Therefore, these manual delamination parameters were selected as the base of comparison.

The push-out and peel-up delamination measurements can be seen in Fig. 8 and Fig. 9, respectively. The images are numbered concerning the number of the experimental runs (listed in Table A1 in the appendices), the original images that were captured after the drilling operation are denoted by the 'o' index, and the images processed with the manual method are denoted by 'm' index, and the images processed with the proposed algorithm are denoted by 'a' index. It can be seen in Figs. 8 and 9, that each of the rough shape and area of the measured delamination are similar to the delaminated areas that can be seen on the original images. These qualitative comparisons suggest that the delamination measurements conducted by the proposed algorithm have similar precision as the manually measured delaminated areas. The results show that each drilling-induced push-out delamination is larger than the peel-up, as was expected based on a generous understanding of delamination formation mechanisms [57]. However, a general tendency is not found whether one of the measurement methods over or lower estimates the expected delamination. This means that the fixed parameters of the proposed method are suitable for delamination measurement because the averages (*i.e.* expected values) of the proposed and manual methods are close to each other. Therefore, the key differences of the measured delaminated zones are quantitatively analysed through the comparisons of F_d, F'_d, $F_{d,inv}$, F_{dmin}, DF, F_{da}, F_{ed} and R_d parameters, below.

Fig. 10 compares the delamination parameters measured by the proposed and manual methods in each analysed delamination parameters, according to **Eq. (21)**.

Table 2
The factors and their levels.

Factors			Levels		
			−1	0	1
Tool geometry	T	-		T1	T2
Cutting speed	v_c	m/min	120	160	200
Feed	f	mm/rev	0.1	0.2	0.3

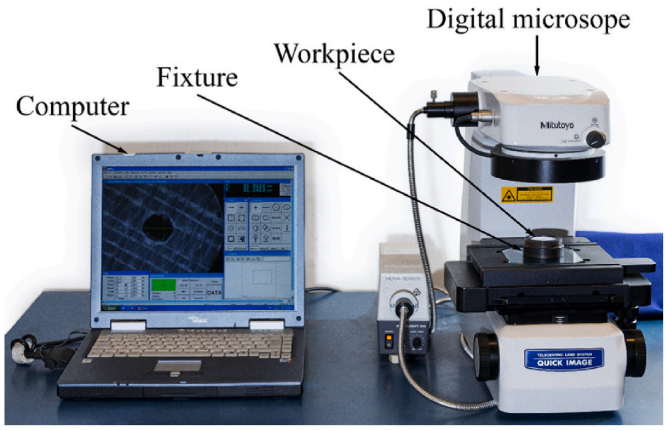

Fig. 7. Image capturing setup.

$$MPD_i = \frac{1}{n}\sum_{i=1}^{n}\frac{DP_{m,i} - DP_{a,i}}{DP_{m,i}} \tag{21}$$

Where MPD denotes the mean percentage difference, DP_m is the manually measured delamination parameter, DP_a is the delamination parameter obtained by the proposed method, and $n = 26$ is the number of experimental runs. The diagram in Fig. 10 shows that the MPD varies between −5.00% and 9.74%, depending on which delamination parameter and which side of the composite is considered. The MPD of the F_{ed} was found to be the lowest (*i.e.* the most precise) and the MPD of F'_d and R_d parameters have the largest values. Nevertheless, MPD of most delamination parameters are below 5%, such as F_d, $F_{d,inv}$, F_{dmin}, DF, F_{da}, F_{ed}. These relatively low MPD values show that the output of the proposed method closely correlates to the manually measured delamination; thus, the proposed method is a well useable (*i.e.* measures accurately compared to the manual method) and automated approach and provides reproducible and comparable delamination parameters. The exit delamination measurements conducted by the proposed method approached the manual results more precisely in most cases (*i.e.* F_d, F'_d, $F_{d,inv}$, F_{dmin}, F_{da}, R_d). The reason for this may be that the peel-up delamination is always smaller and more challenging to model and predict than the push-out one; therefore, the error is proportionally larger. However, the DF and F_{ed} parameter shows a different tendency: the MPD of the exit delamination is larger than the peel-up. Considering that the DF parameter calculates only with the delaminated and nominal hole areas (rather than the diameters of the enclosing circles and nominal hole diameter), and the identification of these areas (*i.e.* each pixel) is more challenging than the outer pixels of the delamination; thus, the nature of its error propagation differs from the other delamination parameters. Nevertheless, the proper reason for this needs further investigation.

The goodness of the proposed method is illustrated by scatterplots of $DP_{m,i}$ versus $DP_{a,i}$, that are shown in Fig. 11. The closer the graph points are to the ideal (red) line, the more similar the results of the two methods are. This similarity is quantitatively characterised by the correlation parameter (r^2), which parameters are shown at the top of the graphs in Fig. 11. The F_d and the R_d delamination parameters performed the best at the entry side ($r^2 = 0.925$), followed by F'_d ($r^2 = 0.924$), F_{da} ($r^2 = 0.906$), $F_{d,inv}$ ($r^2 = 0.890$), F_{dmin} ($r^2 = 0.863$), F_{ed} ($r^2 = 0.654$) and DF ($r^2 = 0.643$), respectively. Nevertheless, the F_{ed} delamination parameter performed the best at the exit side ($r^2 = 0.907$), followed by DF ($r^2 = 0.904$), F_{da} ($r^2 = 0.764$), F_{dmin} ($r^2 = 0.655$), R_d ($r^2 = 0.631$), F'_d ($r^2 = 0.630$), F_d ($r^2 = 0.629$) and $F_{d,inv}$ ($r^2 = 0.570$), respectively. These findings correlate with the content of Fig. 10; thus, the proposed delamination measurement method is suggested to calculate the equivalent delamination factor (F_{ed}) the most precise. However, further improvement of the proposed method is needed, considering the

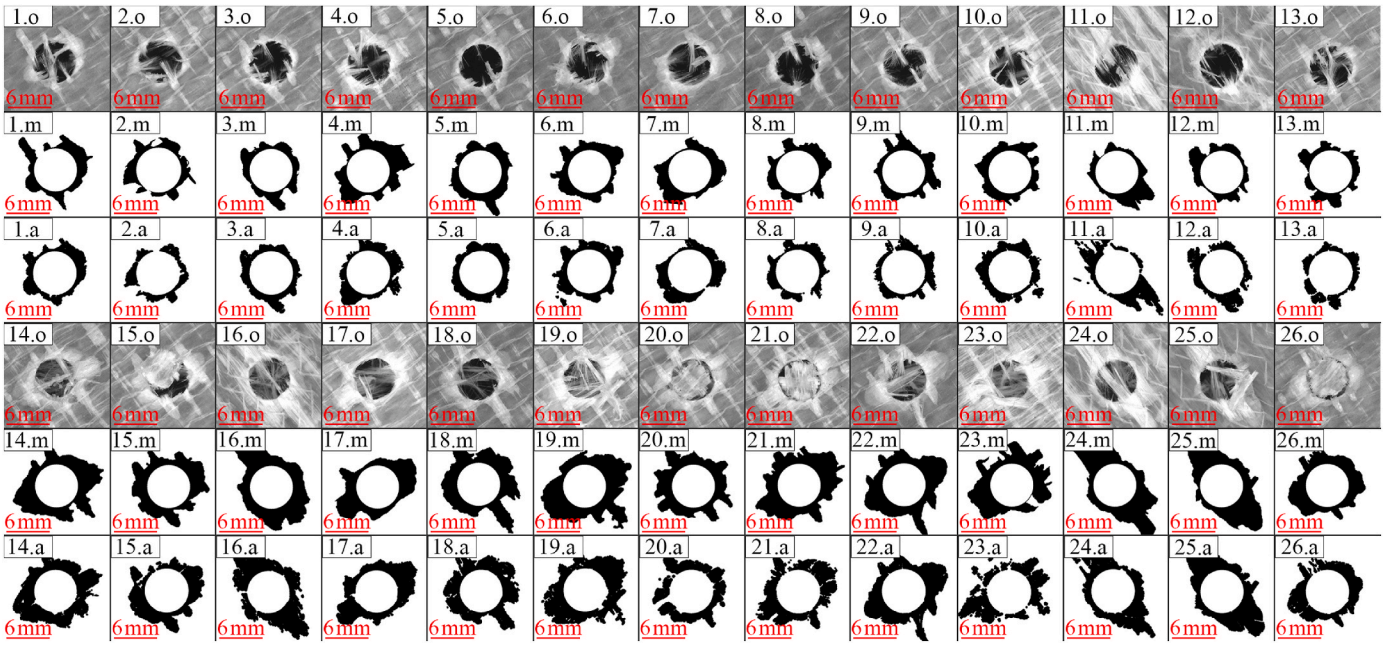

Fig. 8. Push-out delamination measurements in GFRP composite, where 'o' denotes the original images, 'm' denotes the manually measured delamination and 'a' is the output of our proposed algorithm.

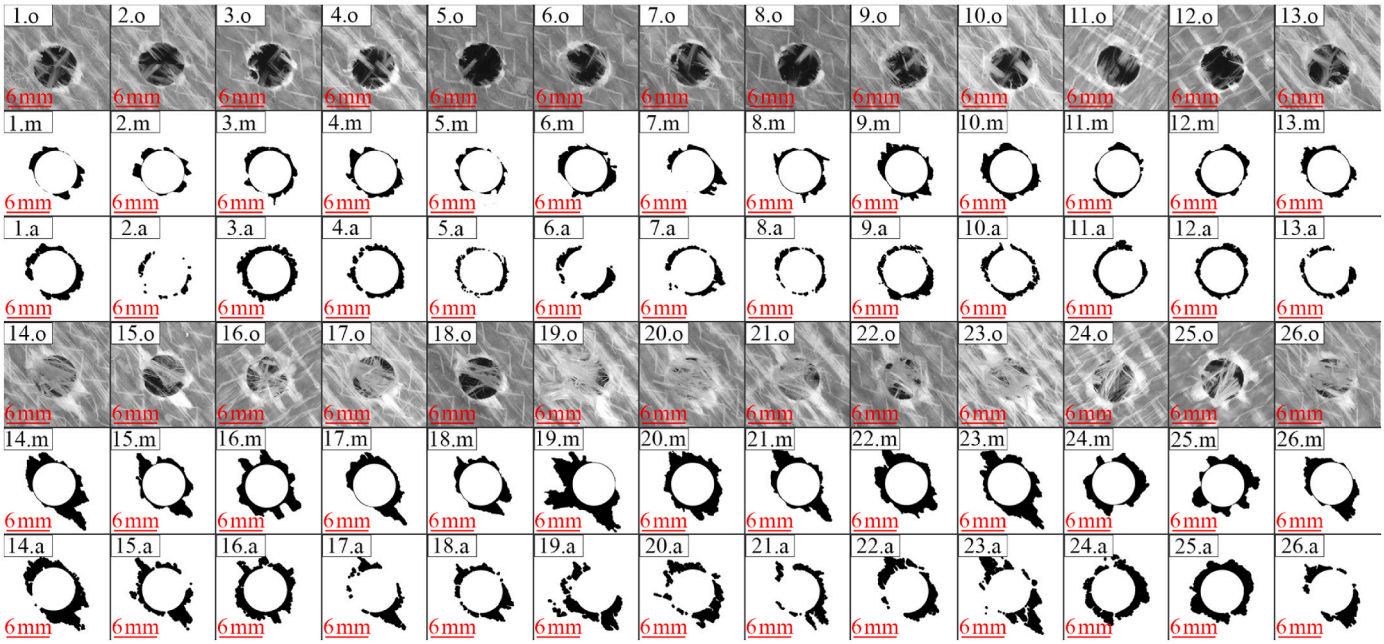

Fig. 9. Peel-up delamination measurements in GFRP composite, where 'o' denotes the original images, 'm' denotes the manually measured delamination and 'a' is the output of our proposed algorithm.

analysed delamination parameters in this study.

Although it is illustrated in Fig. 11 how close each delamination parameter pair is to the nominal red line; these diagrams do not provide information on the means and distributions. Furthermore, the different delamination parameters have different scaling (*e.g.* $F_{d,inv} \in \{0.3 \dots 0.8\}$ and $DF \in \{25 \dots 240\}$); thus, their standardisation is required. Fig. 12 illustrates the gaussian distributions of percentage differences in delamination parameters. The mean of percentage difference of the F_{dmin} (−0.03) was found to be the closest to the nominal (0.00) value at the exit side, followed by the F_{ed} (1.20), F_d (1.27), F'_d (2.07), F_{da} (2.26), R_d (2.35), $F_{d,inv}$ (−2.76) and DF (3.68), respectively. Nevertheless, the F_{ed} was found to have the smallest distribution (3.05), followed by the DF (10.90), F_{da} (12.70), F_{dmin} (12.88), F_d (13.20), $F_{d,inv}$ (13.87), R_d (24.12) and F'_d (24.23), respectively. Considering that the characteristics of the entry (Fig. 12a) and exit (Fig. 12b) delamination parameters are similar, the following can be stated: (i) the delamination parameters measured by the proposed method are close to the manually measured ones in the case of the F_{dmin}, F_{ed} and F_d parameters; (ii) the distribution of F_{ed} was significantly lower than the other delamination parameters. Therefore, the proposed method provides the most accurate result if the equivalent delamination factor (F_{ed}) is applied. The statistical measures of the conventional delamination factor (F_d) are also satisfactory; however, the

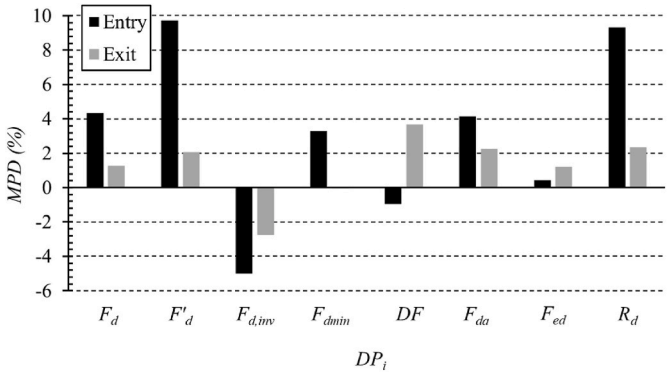

Fig. 10. Comparison of the delamination measurements via different delamination parameters (F_d, F'_d, $F_{d,inv}$, F_{dmin}, DF, F_{da}, F_{ed}, R_d): proposed versus manual method on the entry and exit sides.

measurability of F'_d, DF and R_d parameters are moderate.

5. Discussion

Most of the researchers obtain parameters that are characterising drilling-induced delamination through manual measurements [33–39] or digital image processing (DIP) of images taken by an optical microscope [16,18,32,41,58] and C-scan [42–45]. However, the published measurement methods face considerable deficiencies resulting difficulties. First, these methods often require manual input, that making the processes difficult to automatise and reproduce. Second, the already existing material discontinuities or anomalies (cavities, dirty textured surfaces *etc.*) are not filtered, thus, these are also taken into account when the delamination is quantified. Considering that our proposed method is based on image differencing, it is suitable for detecting material defect caused only by the drilling operation. Furthermore, our method requires no manual input, as each parameter is set through preliminary analysis of images.

Although the main novelty of the proposed method lies in the comparative analysis of surfaces of GFRP composites before and after

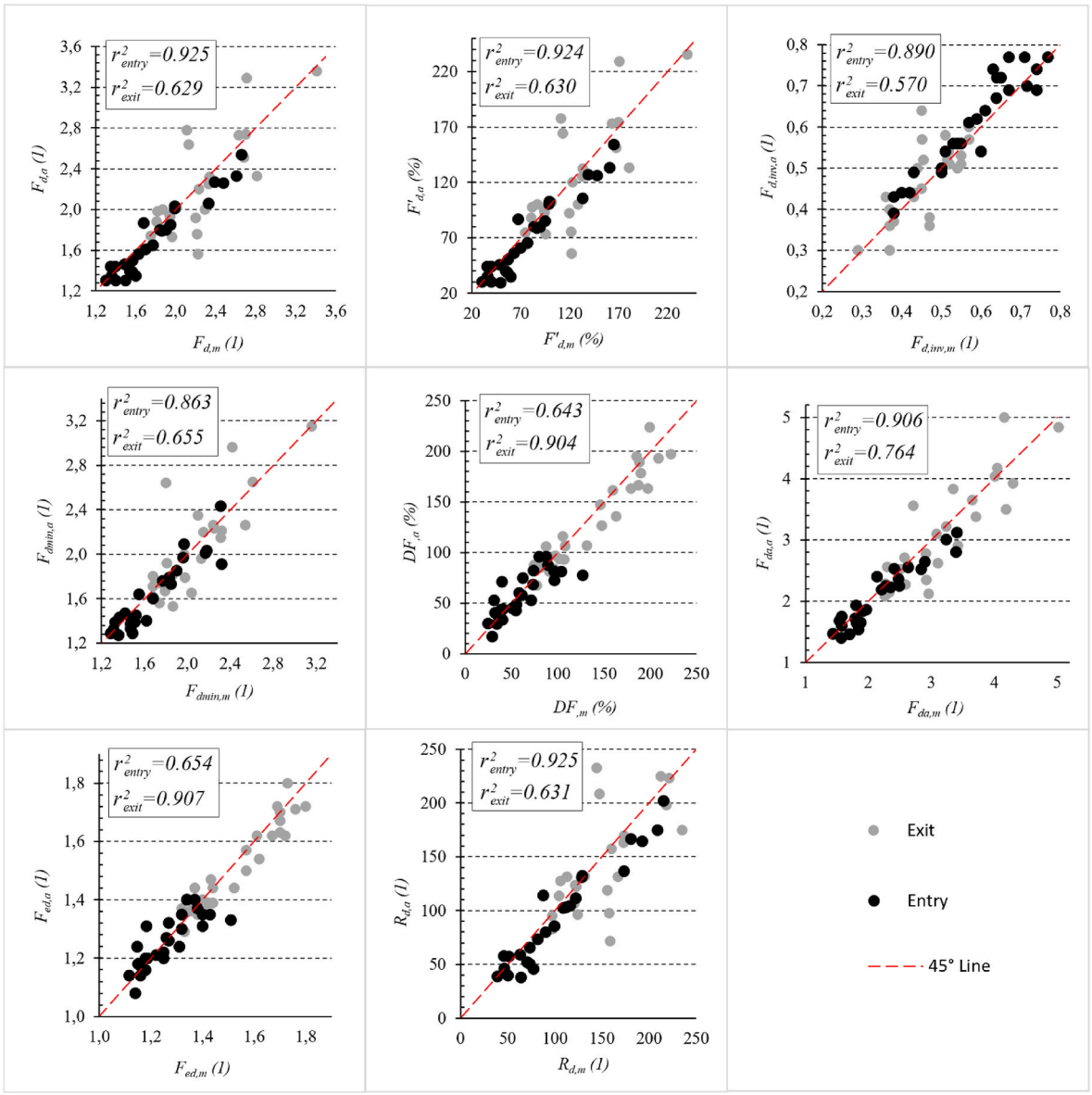

Fig. 11. Scatterplots of delamination parameters measured manually versus by the proposed method: (a) F_d, (b) F'_d, (c) $F_{d,inv}$, (d) F_{dmin}, (e) DF, (f) F_{da}, (g) F_{ed}, (h) R_d.

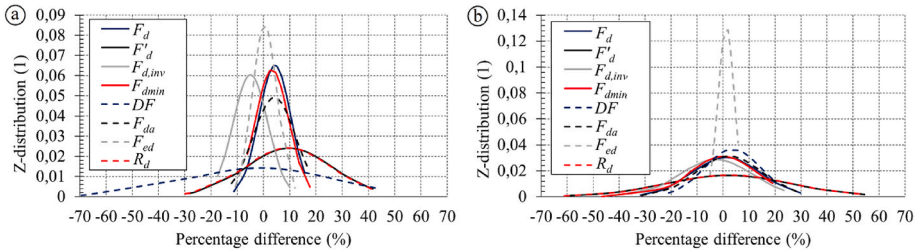

Fig. 12. Gaussian distributions of percentage differences of delamination parameters at the (a) entry and (b) exit sides of the composite.

the drilling operations (*i.e.* image differencing) using existing equipment, and the experimental results are promising; its implementation in industrial environments requires the determination of advantages, disadvantages and limitations, and some further research and development, as discussed respectively below.

The main advantage of the proposed delamination measurement method is that it can measure and separates drilling-induced delamination from other material discontinuities or anomalies (cavities, dirty textured surfaces *etc.*) that are not caused by the drilling operation. In addition, the implementation of this method requires only an industrial camera fixed onto the robotic arm, or spindle head of a machine tool; therefore, it causes no significant investments. However, the operating time of drilling a single hole increases since an image must be taken not only after drilling but also before. Furthermore, if the drilling-induced composite chip (often powder consistency) sticks to the surface of interest, it must be removed by a non-contact method (*e.g.* vacuum) to provide a similar textured surface of interest as it was before the drilling. This may also increase the operation time if the chip removal cannot be solved during the drilling. A further challenge of applying our proposed method is to provide identical lighting conditions during image capturing before and after the drilling. This can be easily solved if the shape of the composite is planar or convex (*e.g.* outer side of the body of an aeroplane). However, the lighting condition of a hole drilled in a concave-shaped composite (*e.g.* inner side of the body of an aeroplane) significantly changes after drilling; therefore, the identical lighting conditions have to be solved by applying a variable brightness lighting device.

One of the main limitations of applying the proposed method is that identical lighting conditions must be provided at each image capturing setup. This means that a variable brightness lighting device has to be applied, and the surface of interest has to be cleaned after drilling to remove the often dusty composite chips. The applicability of the proposed method is tested in glass fibre reinforced polymer composite; thus, it can be used in GFRPs. The applicability in other fibrous composites (*e.g.* CFRP, BFRP, KFRP) needs to be tested and may result in some minor modifications. This is one of our future research directions. It must also be highlighted that although the position and rotation differences of the before and after images are handled by the algorithm, a larger difference may change the lighting conditions significantly, thus increasing noises and errors. Therefore, the position and orientation of the image capturing before and after the drilling should be precise (±1 mm, ±1° accuracy was ensured in this study). The position and orientation differences have to be investigated in the future in order to reach a higher technology readiness level (TRL). Since the proposed method captures two-dimensional images, it is able only to measure the two-dimensional representation of the three-dimensional delamination. Therefore, the current version of the proposed method is not capable of measuring three-dimensional delamination parameters; however, the image differencing principle would be beneficial to use in the future in three-dimensional measurement techniques. Finally, the circle fitting may be challenging if the amount of drilling-induced burrs is significant; therefore, the proposed method is applicable only if the contour of the drilled hole is free of burrs at least on three short circle arcs.

In the future, more significant attention will be shown to the digital image processing of drilling-induced composite defects [5,30,59,60]; therefore, further development of the proposed method is essential to reach sufficient TRL and be useable by industries. Besides, the application range must be widened (other reinforcement types, structures and matrix materials *etc.*) and exactly declared; a detailed investigation is required in the future to deal with a hole with a significant amount of drilling-induced burrs.

6. Conclusions

In the present study, a novel delamination measurement method was developed based on the principle of image differencing. The method is carefully presented and thus can be directly used and post-processed to individual environments. The proposed method does not require complex equipment, unlike CT- or X-ray-based methods, thus it is easy and cost-efficient to implement in the industry. Since the proposed method is based on comparing images captured before and after drilling, the non-drilling-induced material defects do not affect the results. To test the applicability of our proposed method, mechanical drilling experiments were carried out in GFRP composites. 26 holes with a diameter of 6 mm were drilled by varied feed rates, cutting speeds and tools using a back-up plate. Microscopic images were taken of both the entrance and exit sides of the holes and both before and after the drilling operations. The digital images were evaluated by the proposed method and were compared by manual measurements. According to the present study, the following main conclusions can be drawn:

- The proposed delamination measurement method can automatically measure and separate two-dimensional representation of drilling-induced delamination from other material discontinuities or anomalies (cavities, dirty textured surfaces *etc.*) that are not caused by the drilling operation.
- Experimental results show that the output of the proposed method closely correlates to the manually measured delamination till r^2 of 0.925; thus, the proposed method is a well useable (*i.e.* measures accurately compared to the manual method) and automated approach and provides reproducible and comparable delamination parameters.
- The experimental results show that the exit delamination parameters measured by the proposed method are close to the manually measured ones in the case of the equivalent delamination factor (r^2 of F_{ed} is 0.907). The distribution of F_{ed} (1.20) was significantly lower than the other delamination parameters analysed in this study (till 24.23). Therefore, the proposed method provides the most accurate result if the equivalent delamination factor is applied at the hole exit. The statistical measures of the conventional delamination factor (F_d) are satisfactory (*i.e.* r^2 of F_d is 0.925) at the hole entry; however, the measurability of F'_d, DF and R_d parameters are moderate at both entry and exit of the holes.
- The implementation of the proposed method in the industrial environment causes no significant investments; however, the operating time of drilling a single hole increases since an image must be taken not only after drilling but also before. Furthermore, identical lighting conditions are needed during image capturing before and after the

drilling. The principle of the proposed method may capable of three-dimensional measurements by repeating on discrete z-layers.

It was proved that the proposed delamination measurement method is useable in GFRP composites; however, its applicability in other fibrous composites (*e.g.* CFRP, BFRP, KFRP) needs to be tested in the future.

CRediT authorship contribution statement

Tamas Lukacs: Data curation, Formal analysis, Investigation, Methodology, Software, Writing – original draft. **Csongor Pereszlai:** Conceptualization, Methodology, Visualization. **Norbert Geier:** Methodology, Investigation, Supervision, Writing – review & editing.

Declaration of competing interest

The authors declare that they have no known competing financial interests or personal relationships that could have appeared to influence the work reported in this paper.

Data availability

Data will be made available on request.

Acknowledgements

The research reported in this paper and carried out at BME has been supported by the National Laboratory of Artificial Intelligence funded by the NRDIO under the auspices of the Ministry for Innovation and Technology, and by the János Bolyai Research Scholarship of the Hungarian Academy of Sciences No. BO/00508/22/6. The authors acknowledge the support of Dániel István Poór in the experimental work.

Appendices.

Table A1
Measured push-out delamination values by the proposed algorithm

No. (−)	v_c (m/min)	f (mm/rev)	T (−)	F_d (−)	F_d' (−)	$F_{d,inv}$ (−)	F_{dmin} (−)	DF (−)	F_{da} (−)	F_{ed} (−)	R_d (−)
1	160	0.3	T1	1.76	75.57	0.57	1.65	93.54	2.35	1.39	97.49
2	200	0.1	T1	1.66	65.63	0.60	1.56	67.28	2.08	1.29	85.97
3	160	0.2	T1	1.93	93.22	0.52	1.74	88.50	2.52	1.37	122.12
4	160	0.2	T1	1.92	92.21	0.52	1.79	106.71	2.62	1.44	118.95
5	160	0.1	T1	1.56	55.59	0.64	1.53	93.19	2.12	1.39	71.71
6	120	0.3	T1	2.00	100.28	0.50	1.92	106.49	2.71	1.44	131.37
7	200	0.2	T1	1.85	84.62	0.54	1.74	116.20	2.60	1.47	106.62
8	120	0.1	T1	1.64	63.94	0.61	1.62	81.06	2.14	1.35	83.13
9	200	0.3	T1	1.73	73.39	0.58	1.67	84.14	2.27	1.36	96.14
10	160	0.2	T1	1.88	87.99	0.53	1.76	96.83	2.51	1.40	113.51
11	160	0.2	T1	2.78	177.66	0.36	2.64	105.84	3.56	1.44	232.74
12	160	0.2	T1	1.98	97.47	0.51	1.80	87.57	2.56	1.37	127.69
13	120	0.2	T1	1.74	74.42	0.57	1.71	85.33	2.29	1.36	95.25
14	160	0.15	T2	2.32	132.39	0.43	2.23	189.26	3.65	1.70	169.46
15	200	0.05	T2	2.02	102.27	0.49	2.00	161.25	3.10	1.62	131.93
16	160	0.1	T2	3.29	229.08	0.30	2.96	223.72	5.00	1.80	295.51
17	160	0.1	T2	2.20	120.21	0.45	2.20	147.33	3.22	1.57	157.47
18	160	0.05	T2	2.33	133.37	0.43	2.26	166.61	3.50	1.63	174.71
19	120	0.15	T2	2.51	151.17	0.40	2.21	197.00	3.92	1.72	198.03
20	200	0.1	T2	2.00	100.19	0.50	1.96	135.82	2.91	1.54	131.25
21	120	0.05	T2	2.25	125.40	0.44	2.15	162.99	3.38	1.62	163.02
22	200	0.15	T2	2.73	173.11	0.37	2.26	178.42	4.04	1.67	225.05
23	160	0.1	T2	2.64	164.19	0.38	2.35	163.34	3.83	1.62	208.52
24	160	0.1	T2	3.36	235.54	0.30	3.15	193.10	4.84	1.71	303.84
25	160	0.1	T2	2.74	174.41	0.36	2.65	194.62	4.17	1.72	223.24
26	120	0.1	T2	1.94	94.29	0.51	1.81	126.42	2.78	1.50	123.52

Table A2
Measured peel-up delamination values by the proposed algorithm.

No. (−)	v_c (m/min)	f (mm/rev)	T (−)	F_d (−)	F_d' (−)	$F_{d,inv}$ (−)	F_{dmin} (−)	DF (−)	F_{da} (−)	F_{ed} (−)	R_d (−)
1	160	0.3	T1	1.44	43.98	0.70	1.43	52.67	1.75	1.24	57.18
2	200	0.1	T1	1.30	30.16	0.77	1.27	16.80	1.40	1.08	39.51
3	160	0.2	T1	1.50	50.35	0.67	1.47	70.90	1.93	1.31	65.46
4	160	0.2	T1	1.39	38.65	0.72	1.37	44.16	1.64	1.20	50.63
5	160	0.1	T1	1.30	30.21	0.77	1.29	29.67	1.47	1.14	38.97
6	120	0.3	T1	1.46	45.55	0.69	1.43	45.12	1.72	1.21	59.22
7	200	0.2	T1	1.61	60.82	0.62	1.45	37.93	1.84	1.17	79.67
8	120	0.1	T1	1.30	29.49	0.77	1.29	29.28	1.46	1.14	38.05
9	200	0.3	T1	1.56	56.13	0.64	1.40	48.62	1.86	1.22	73.53
10	160	0.2	T1	1.40	39.93	0.72	1.39	42.80	1.65	1.20	52.31
11	160	0.2	T1	1.44	44.25	0.69	1.39	40.19	1.68	1.18	57.97
12	160	0.2	T1	1.35	35.16	0.74	1.32	43.61	1.60	1.20	46.06
13	120	0.2	T1	1.35	34.75	0.74	1.33	33.74	1.54	1.16	45.52
14	160	0.15	T2	2.33	133.39	0.43	2.03	95.80	3.01	1.40	174.74
15	200	0.05	T2	2.03	102.61	0.49	1.97	74.79	2.53	1.32	132.37

(*continued on next page*)

Table A2 (*continued*)

No. (−)	v_c (m/min)	f (mm/rev)	T (−)	F_d (−)	F_d' (−)	$F_{d,inv}$ (−)	F_{dmin} (−)	DF (−)	F_{da} (−)	F_{ed} (−)	R_d (−)
16	160	0.1	T2	1.80	79.80	0.56	1.73	87.75	2.36	1.37	104.54
17	160	0.1	T2	2.27	126.95	0.44	2.09	52.75	2.64	1.24	166.30
18	160	0.05	T2	1.80	80.15	0.56	1.76	60.30	2.19	1.27	102.59
19	120	0.15	T2	2.26	126.32	0.44	1.91	77.54	2.80	1.33	164.22
20	200	0.1	T2	1.79	78.77	0.56	1.77	72.39	2.25	1.31	103.18
21	120	0.05	T2	2.06	105.79	0.49	2.01	68.34	2.52	1.30	136.47
22	200	0.15	T2	2.01	100.65	0.50	1.85	81.59	2.55	1.35	130.85
23	160	0.1	T2	2.54	154.01	0.39	2.43	81.15	3.12	1.35	201.76
24	160	0.1	T2	1.87	86.97	0.54	1.64	81.93	2.40	1.35	113.93
25	160	0.1	T2	1.65	65.22	0.61	1.60	95.97	2.25	1.40	85.43
26	120	0.1	T2	1.85	85.20	0.54	1.79	57.95	2.23	1.26	111.62

References

[1] Geier N, Paulo Davim J, Szalay T. Advanced cutting tools and technologies for drilling carbon fibre reinforced polymer (CFRP) composites: a review. Compos Appl Sci Manuf 2019;125:105552. https://doi.org/10.1016/j.compositesa.2019.105552.

[2] Altin Karatas M, Gökkaya H. A review on machinability of carbon fiber reinforced polymer (CFRP) and glass fiber reinforced polymer (GFRP) composite materials. Defence Technology; 2018. https://doi.org/10.1016/j.dt.2018.02.001.

[3] Arias GG, Díaz FJ, Ramírez ER, Guzman JV. Thermal analysis by finite elements of Hotends for 3D Printing by fused filament fabrication. Period Polytech - Mech Eng 2021;65:129–33. https://doi.org/10.3311/PPme.16203.

[4] Xu J, An Q, Chen M. A comparative evaluation of polycrystalline diamond drills in drilling high-strength T800S/250F CFRP. Compos Struct 2014;117:71–82. https://doi.org/10.1016/j.compstruct.2014.06.034.

[5] István Poór D, Geier N, Pereszlai C, Xu J. A critical review of the drilling of CFRP composites: burr formation, characterisation and challenges. Compos B Eng 2021:109155. https://doi.org/10.1016/j.compositesb.2021.109155.

[6] Anand RS, Patra K. Mechanistic cutting force modelling for micro-drilling of CFRP composite laminates. CIRP J Manuf Sci Technol 2017;16:55–63. https://doi.org/10.1016/j.cirpj.2016.07.002.

[7] Davim JP. Machining composites materials. John Wiley & Sons; 2013.

[8] Davim JP. Machining: fundamentals and recent advances. Springer Science & Business Media; 2008.

[9] Krishnaraj V, Zitoune R, Davim JP. Drilling of polymer-matrix composites. Berlin, Heidelberg: Springer Berlin Heidelberg; 2013. https://doi.org/10.1007/978-3-642-38345-8.

[10] Hegedus G, Sarkadi T, Czigany T. Self-sensing composite: reinforcing fiberglass bundle for damage detection. Compos Appl Sci Manuf 2020;131:105804. https://doi.org/10.1016/j.compositesa.2020.105804.

[11] Kumar Panchagnula K, Vamsi Krishna Jasti N, Sharma Panchagnula J. Prediction of drilling induced delamination and circularity deviation in GFRP nanocomposites using deep neural network. Mater Today Proc 2022. https://doi.org/10.1016/j.matpr.2022.02.041.

[12] Ali HM, Iqbal A, Liang L. A comparative study on the use of drilling and milling processes in hole making of GFRP composite. Sadhana 2013;38:743–60. https://doi.org/10.1007/s12046-013-0186-5.

[13] Monoranu M, Mitchell RL, Kerrigan K, Fairclough JPA, Ghadbeigi H. The effect of particle reinforcements on chip formation and machining induced damage of modified epoxy carbon fibre reinforced polymers (CFRPs). Compos Appl Sci Manuf 2022;154:106793. https://doi.org/10.1016/j.compositesa.2021.106793.

[14] Geng D, Liu Y, Shao Z, Lu Z, Cai J, Li X, et al. Delamination formation, evaluation and suppression during drilling of composite laminates: a review. Compos Struct 2019;216:168–86. https://doi.org/10.1016/j.compstruct.2019.02.099.

[15] Babu J, Sunny T, Paul NA, Mohan KP, Philip J, Davim JP. Assessment of delamination in composite materials: a review. Proc IME B J Eng Manufact 2016;230:1990–2003. https://doi.org/10.1177/0954405415619343.

[16] Gaugel S, Sripathy P, Haeger A, Meinhard D, Bernthaler T, Lissek F, et al. A comparative study on tool wear and laminate damage in drilling of carbon-fiber reinforced polymers (CFRP). Compos Struct 2016;155:173–83. https://doi.org/10.1016/j.compstruct.2016.08.004.

[17] Liu L, Qi C, Wu F, Zhang X, Zhu X. Analysis of thrust force and delamination in drilling GFRP composites with candle stick drills. Int J Adv Manuf Technol 2018;95:2585–600. https://doi.org/10.1007/s00170-017-1369-8.

[18] Sorrentino L, Turchetta S, Bellini C. A new method to reduce delaminations during drilling of FRP laminates by feed rate control. Compos Struct 2018;186:154–64. https://doi.org/10.1016/j.compstruct.2017.12.005.

[19] Lissek F, Tegas J, Kaufeld M. Damage quantification for the machining of CFRP: an introduction about characteristic values considering shape and orientation of drilling-induced delamination. Procedia Eng 2016;149:2–16. https://doi.org/10.1016/j.proeng.2016.06.632.

[20] Hocheng H, Tsao CC. The path towards delamination-free drilling of composite materials. J Mater Process Technol 2005;167:251–64. https://doi.org/10.1016/j.jmatprotec.2005.06.039.

[21] Wang F, Yin J, Ma J, Jia Z, Yang F, Niu B. Effects of cutting edge radius and fiber cutting angle on the cutting-induced surface damage in machining of unidirectional CFRP composite laminates. Int J Adv Manuf Technol 2017;91:3107–20. https://doi.org/10.1007/s00170-017-0023-9.

[22] Biro I, Szalay T. Extension of empirical specific cutting force model for the process of fine chip-removing milling. Int J Adv Manuf Technol 2017;88:2735–43. https://doi.org/10.1007/s00170-016-8957-x.

[23] Balázs BZ, Geier N, Takács M, Davim JP. A review on micro-milling: recent advances and future trends. Int J Adv Manuf Technol 2021;112:655–84. https://doi.org/10.1007/s00170-020-06445-w.

[24] Balázs BZ, Takács M. Experimental investigation of surface characteristics and dynamic effects at micro milling of hardened hot-work tool steel. IJMMM 2020;22:504. https://doi.org/10.1504/IJMMM.2020.111355.

[25] Chen T, Gao F, Li S, Liu X. Experimental study on cutting tool wear in milling carbon fiber composites with spiral staggered diamond-coated milling cutter. Int J Adv Manuf Technol 2018;98:413–9. https://doi.org/10.1007/s00170-018-2297-y.

[26] Ashworth S, Fairclough JPA, Takikawa Y, Scaife R, Ghadbeigi H, Kerrigan K, et al. Effects of machine stiffness and cutting tool design on the surface quality and flexural strength of edge trimmed carbon fibre reinforced polymers. Compos Appl Sci Manuf 2019;119:88–100. https://doi.org/10.1016/j.compositesa.2019.01.019.

[27] Dogrusadik A, Kentli A. Comparative assessment of support plates' influences on delamination damage in micro-drilling of CFRP laminates. Compos Struct 2017;173:156–67. https://doi.org/10.1016/j.compstruct.2017.04.031.

[28] Dogrusadik A, Kentli A. Experimental investigation of support plates' influences on tool wear in micro-drilling of CFRP laminates. J Manuf Process 2019;38:214–22. https://doi.org/10.1016/j.jmapro.2019.01.018.

[29] Yazman Ş. The effects of back-up on drilling machinability of filament wound GFRP composite pipes: mechanical characterization and drilling tests. J Manuf Process 2021;68:1535–52. https://doi.org/10.1016/j.jmapro.2021.06.054.

[30] Geier N, Xu J, Pereszlai C, Poór DI, Davim JP. Drilling of carbon fibre reinforced polymer (CFRP) composites: difficulties, challenges and expectations. Procedia Manuf 2021;54:284–9. https://doi.org/10.1016/j.promfg.2021.07.045.

[31] Geier N, Szalay T. Optimisation of process parameters for the orbital and conventional drilling of uni-directional carbon fibre-reinforced polymers (UD-CFRP). Measurement 2017;110:319–34. https://doi.org/10.1016/j.measurement.2017.07.007.

[32] Davim JP, Rubio JC, Abrao AM. A novel approach based on digital image analysis to evaluate the delamination factor after drilling composite laminates. Compos Sci Technol 2007;67:1939–45. https://doi.org/10.1016/j.compscitech.2006.10.009.

[33] Franke V. Drilling of long fiber reinforced thermoplastics—influence of the cutting edge on the machining results. CIRP Ann 2011;60:65–8. https://doi.org/10.1016/j.cirp.2011.03.078.

[34] Hintze W, Hartmann D, Schütte C. Occurrence and propagation of delamination during the machining of carbon fibre reinforced plastics (CFRPs) – an experimental study. Compos Sci Technol 2011;71:1719–26. https://doi.org/10.1016/j.compscitech.2011.08.002.

[35] Davim JP, Reis P. Drilling carbon fiber reinforced plastics manufactured by autoclave—experimental and statistical study. Mater Des 2003;24:315–24. https://doi.org/10.1016/S0261-3069(03)00062-1.

[36] Davim JP, Reis P. Study of delamination in drilling carbon fiber reinforced plastics (CFRP) using design experiments. Compos Struct 2003;59:481–7. https://doi.org/10.1016/S0263-8223(02)00257-X.

[37] Ünüvar A, Koyunbakan M, Bagci M. Optimization and effects of machining parameters on delamination in drilling of pure and Al2O3/SiO2-added GFRP composites. Int J Adv Manuf Technol 2022;119:657–75. https://doi.org/10.1007/s00170-021-08258-x.

[38] Gaitonde VN, Karnik SR, Rubio JC, Correia AE, Abrão AM, Davim JP. A study aimed at minimizing delamination during drilling of CFRP composites. J Compos Mater 2011;45:2359–68. https://doi.org/10.1177/0021998311401087.

[39] Abrão AM, Rubio JCC, Faria PE, Davim JP. The effect of cutting tool geometry on thrust force and delamination when drilling glass fibre reinforced plastic composite. Mater Des 2008;29:508–13. https://doi.org/10.1016/j.matdes.2007.01.016.

[40] Gaitonde VN, Karnik SR, Rubio JC, Correia AE, Abrão AM, Davim JP. Analysis of parametric influence on delamination in high-speed drilling of carbon fiber reinforced plastic composites. J Mater Process Technol 2008;203:431–8. https://doi.org/10.1016/j.jmatprotec.2007.10.050.

[41] Hrechuk A, Bushlya V, Ståhl J-E. Hole-quality evaluation in drilling fiber-reinforced composites. Compos Struct 2018;204:378–87. https://doi.org/10.1016/j.compstruct.2018.07.105.
[42] Tsao CC, Hocheng H. Computerized tomography and C-Scan for measuring delamination in the drilling of composite materials using various drills. Int J Mach Tool Manufact 2005;45:1282–7. https://doi.org/10.1016/j.ijmachtools.2005.01.009.
[43] Gaudenzi P, Bernabei M, Dati E, De Angelis G, Marrone M, Lampani L. On the evaluation of impact damage on composite materials by comparing different NDI techniques. Compos Struct 2014;118:257–66. https://doi.org/10.1016/j.compstruct.2014.07.048.
[44] Dong J, Kim B, Locquet A, McKeon P, Declercq N, Citrin DS. Nondestructive evaluation of forced delamination in glass fiber-reinforced composites by terahertz and ultrasonic waves. Compos B Eng 2015;79:667–75. https://doi.org/10.1016/j.compositesb.2015.05.028.
[45] Xu J, Li C, Mi S, An Q, Chen M. Study of drilling-induced defects for CFRP composites using new criteria. Compos Struct 2018;201:1076–87. https://doi.org/10.1016/j.compstruct.2018.06.051.
[46] Geier N, Poór DI, Pereszlai C, Bacs J, Balázs BZ. Fúrásindukált delamináció kialakulása és mérőszámai szálerősített polimer (FRP) kompozitokban. Gradus 2021;8:254–60. https://doi.org/10.47833/2021.1.ENG.005.
[47] Chen W-C. Some experimental investigations in the drilling of carbon fiber-reinforced plastic (CFRP) composite laminates. Int J Mach Tool Manufact 1997;37:1097–108. https://doi.org/10.1016/S0890-6955(96)00095-8.
[48] Khanna N, Pusavec F, Agrawal C, Krolczyk GM. Measurement and evaluation of hole attributes for drilling CFRP composites using an indigenously developed cryogenic machining facility. Measurement 2020;154:107504. https://doi.org/10.1016/j.measurement.2020.107504.
[49] Silva DNR da. Image processing methodology for assessment of drilling induced damage in CFRP. masterThesis. Faculdade de Ciências e Tecnologia; 2013.
[50] Faraz A, Biermann D, Weinert K. Cutting edge rounding: an innovative tool wear criterion in drilling CFRP composite laminates. Int J Mach Tool Manufact 2009;49:1185–96. https://doi.org/10.1016/j.ijmachtools.2009.08.002.
[51] Tsao CC, Kuo KL, Hsu IC. Evaluation of a novel approach to a delamination factor after drilling composite laminates using a core–saw drill. Int J Adv Manuf Technol 2012;59:617–22. https://doi.org/10.1007/s00170-011-3532-y.
[52] Khashaba UA. Delamination in drilling GFR-thermoset composites. International Conference on Aerospace Sciences and Aviation Technology 2003;10:461–81. https://doi.org/10.21608/asat.2013.24453.
[53] Maghami A, Salehi M, Khoshdarregi M. Automated vision-based inspection of drilled CFRP composites using multi-light imaging and deep learning. CIRP J Manuf Sci Technol 2021;35:441–53. https://doi.org/10.1016/j.cirpj.2021.07.015.
[54] Afify HA. Evaluation of change detection techniques for monitoring land-cover changes: a case study in new Burg El-Arab area. Alex Eng J 2011;50:187–95. https://doi.org/10.1016/j.aej.2011.06.001.
[55] Luo D, Smart P, Macleod JES. Circular hough transform for roundness measurement of objects. Pattern Recogn 1995;28:1745–9. https://doi.org/10.1016/0031-3203(95)00045-2.
[56] Wang S, Li W, Yuan Z, Jin Q, Ding Z, Liu X, et al. Semiquantitative naked-eye detection of synthetic food colorants using highly-branched pipette tip as an all-in-one device. Anal Chim Acta 2022;1211:339901. https://doi.org/10.1016/j.aca.2022.339901.
[57] Fu Q, Wu S, Li C, Xu J, Wang D. Delamination and chip breaking mechanism of orthogonal cutting CFRP/Ti6Al4V composite. J Manuf Process 2022;73:183–96. https://doi.org/10.1016/j.jmapro.2021.11.015.
[58] Campos Rubio J, Abrao AM, Faria PE, Correia AE, Davim JP. Effects of high speed in the drilling of glass fibre reinforced plastic: evaluation of the delamination factor. Int J Mach Tool Manufact 2008;48:715–20. https://doi.org/10.1016/j.ijmachtools.2007.10.015.
[59] Cepero-Mejías F, Curiel-Sosa JL, Blázquez A, Yu TT, Kerrigan K, Phadnis VA. Review of recent developments and induced damage assessment in the modelling of the machining of long fibre reinforced polymer composites. Compos Struct 2020;240:112006. https://doi.org/10.1016/j.compstruct.2020.112006.
[60] Geier N, Póka G, Jacsó Á, Pereszlai C. A method to predict drilling-induced burr occurrence in chopped carbon fibre reinforced polymer (CFRP) composites based on digital image processing. Compos B Eng 2022;242:110054. https://doi.org/10.1016/j.compositesb.2022.110054.